Commun. Comput. Phys.
doi: 10.4208/cicp.080509.310310s

Vol. **9**, No. 3, pp. 711-739
March 2011

Adaptive Conservative Cell Average Spectral Element Methods for Transient Wigner Equation in Quantum Transport

Sihong Shao[1], Tiao Lu[1] and Wei Cai[2,*]

[1] *LMAM and School of Mathematical Sciences, Peking University, Beijing 100871, China.*
[2] *Department of Mathematics and Statistics, University of North Carolina at Charlotte, Charlotte, NC 28223, USA.*

Received 8 May 2009; Accepted (in revised version) 31 March 2010

Available online 17 September 2010

To the memory of David Gottlieb

Abstract. A new adaptive cell average spectral element method (SEM) is proposed to solve the time-dependent Wigner equation for transport in quantum devices. The proposed cell average SEM allows adaptive non-uniform meshes in phase spaces to reduce the high-dimensional computational cost of Wigner functions while preserving exactly the mass conservation for the numerical solutions. The key feature of the proposed method is an analytical relation between the cell averages of the Wigner function in the k-space (local electron density for finite range velocity) and the point values of the distribution, resulting in fast transforms between the local electron density and local fluxes of the discretized Wigner equation via the fast sine and cosine transforms. Numerical results with the proposed method are provided to demonstrate its high accuracy, conservation, convergence and a reduction of the cost using adaptive meshes.

AMS subject classifications: 65M70, 65M50, 42B20, 45K05, 81Q05

Key words: Wigner equation, quantum transport, spectral element methods, adaptive mesh.

1 Introduction

Ever since its invention in 1932 by Wigner in [1], the Wigner equation has found applications in many physical fields, such as optics, information theory and statistical physics and has constituted a new formulation of quantum mechanics [2,3]. The most appealing characteristic of the Wigner equation is that it describes the evolution of quantum states

*Corresponding author. *Email addresses:* shaosihong@gmail.com (S. Shao), tlu@math.pku.edu.cn (T. Lu), wcai@uncc.edu (W. Cai)

in the same way as the Boltzmann equation does for classical systems. Both of them are defined in a phase space and a physical interpretation can be given to terms appearing in their dynamical equations. Although it is not a real probability distribution function due to possible negative values as a result of the Heisenberg uncertainty principle, the Wigner function serves the role of a distribution [4,5], for example, in calculating number densities, current densities and etc. Using the Wigner equation to investigate quantum transport has become more popular [6,7] when the quantum behavior of semiconductor devices can not be neglected as their size is down to nano-scales.

Frensley succeeded in simulating the quantum transport in a resonant tunneling diode (RTD) by solving the Wigner equation with a first-order upwind scheme finite difference method (FDM) [8,9]. Since then, several second-order FDMs have been used [10] (for a detailed summary about FDMs for the Wigner equation, please refer to [11,12]). It has been shown that general FDMs are not very accurate for transient Wigner simulations and questions have been raised about the effect of the finite difference discretization of inflow/outflow boundary conditions proposed by Frensley in [9]. Moreover, in order to include the space charge effect, the Wigner equation should be coupled with a Poisson equation [13,14] and a self-consistent iteration is needed to solve the coupled system. Application of such models with FDM solvers can be found in [15–17] where the time-independent Wigner-Poisson system is considered. Recently, the Wigner function is extended to particle modeling accounting for various kinds of scatterings [18], where the Boltzmann equation and the Wigner equation are coupled in a unified framework so that simulation of actual quantum transport can be achieved by Monte Carlo methods [19,20].

In [21,22] a spectral method based on plane waves is used to discretize the transient Wigner equation in the k-space while FDMs are used in the x-space. In [23,24] an operator splitting method is used to calculate the coupled Wigner-Poisson system. The reason for using plane wave spectral methods is that the plane waves are the eigenfunctions of the pseudo-differential operator associated with the Wigner potentials. However, there are several issues in approximating the Wigner distributions in the k-space with periodic plane waves. The periodization in the k-space produces a numerical solution which resides in a different function space (periodic function) other than the original Wigner function space $L^2(-\infty,\infty)$ and more importantly, creates an unphysical interaction of the Wigner distribution with its periodic image frequencies in the k-space. Mathematically speaking, we need to handle carefully the infinite integral with respect to the dual variable y appearing in the pseudo-differential operator $\Theta_V[f]$ of (2.4). In [25,26], after assuming that $\widehat{f}(x,y,t)$ defined in (2.5) has a compact support in the y-space with a truncated domain in the y-space as $[-1/(2\Delta k),1/(2\Delta k)]$, the authors showed that the semi-discretized Wigner equation–finite difference discretization in the k-space in a uniform mesh–is well-posed and approaches the continuous problem when the mesh size Δk goes to zero.

Our main objective in this paper is to reduce the cost of computing the Wigner distribution in high-dimensional phase spaces. For this purpose, adaptive meshes will be our approach which concentrates the computational resources in regions of localized electron

density while still maintaining the electron conservation for the numerical solutions. A new adaptive spectral element method (SEM) is thus proposed by using both cell averages and point values of the Wigner distribution function in the integro-differential Wigner equation. To achieve the efficiency of the method, we will take advantage of the fact [27, 28] that, for any function $u(k)$ in the space of the trigonometric plane waves or the Chebyshev polynomials, there is an exact relation between its cell averages and point values. This relation allows us to determine the expansion coefficients of the numerical solution with a Chebyshev collocation method for local continuity equations, in an efficient manner with the help of fast sine and cosine transforms. More importantly, we can show that the electron conservation for the numerical solution is maintained analytically even with non-uniform adaptive meshes in the phase space. The proposed cell average SEM achieves the optimal efficiency with the help of fast Fourier transforms when Gauss-Chebyshev points in the k-space and Gauss-Lobatto points in the x-space are used in the collocation approximation of the continuity equations. With the multi-step Runge-Kutta time discretization [29], high-order, conservative, stable and efficient numerical methods for the transient Wigner simulation are obtained.

The rest of the paper is organized as follows. In Section 2, we introduce the Wigner equation with discussion of several issues related to the numerical methods such as truncation of the phase space, mass conservation and boundary conditions. In Section 3, we construct the conservative cell average SEM and also its p-adaptive strategy. Section 4 conducts numerical experiments to demonstrate the accuracy and capability of the proposed method. Concluding remarks and some discussions are given in Section 5.

2 Wigner equations

The Wigner function $f(x,k,t)$ for a one-dimensional quantum device is defined in the phase space $(x,k)\in\mathbb{R}^2$ for the position x and the wave number k through a Fourier transform in the difference coordinates of the density operator $\rho(x,x',t)$. The density operator is a Gibbs ensemble average (denoted by the overbar) of the wave functions $\psi(x,t)$ for the quantum system under consideration [30]

$$\rho(x,x',t)=\overline{\psi(x,t)\psi^*(x',t)}, \tag{2.1}$$

and by using the Weyl-Wigner transform of the density operator, we define

$$f(x,k,t)=\int_{-\infty}^{+\infty}\exp(-\mathrm{i}ky)\rho\Big(x+\frac{y}{2},x-\frac{y}{2},t\Big)\,\mathrm{d}y. \tag{2.2}$$

The Wigner function $f(x,k,t)$ satisfies the following transient Wigner equation

$$\frac{\partial}{\partial t}f(x,k,t)+\frac{\hbar k}{m}\frac{\partial}{\partial x}f(x,k,t)=\Theta_V[f](x,k,t), \tag{2.3}$$

where the right hand side is the so-called Vlasov-Wigner pseudo-differential operator,

$$\Theta_V[f](x,k,t)=\frac{\mathrm{i}}{\hbar}\int_{-\infty}^{+\infty}\exp(-\mathrm{i}ky)D_V(x,y)\widehat{f}(x,y,t)\mathrm{d}y:=\frac{\mathrm{i}}{\hbar}\mathcal{F}[D_V\widehat{f}](x,k,t), \tag{2.4}$$

and m is the effective mass of the electron, $\hbar$ is the reduced Planck constant. Here, $V(x)$ is the potential, $D_V(x,y)$ is the potential difference in the difference coordinate,

$$D_V(x,y)=V\left(x-\frac{y}{2}\right)-V\left(x+\frac{y}{2}\right),$$

and $\widehat{f}(x,y,t)$ is just another notation for $\rho(x+y/2,x-y/2,t)$ from (2.2) through another Fourier transform for the k-variable,

$$\widehat{f}(x,y,t)=\frac{1}{2\pi}\int_{-\infty}^{+\infty}\exp(\mathrm{i}ky)f(x,k,t)\mathrm{d}k:=\mathcal{F}^{-1}[f](x,y,t). \tag{2.5}$$

It has been shown that in [31], the L^2-norm of Wigner function $f(x,k,t)$ is time invariant for L^2 initial data and bounded potential and so does $\widehat{f}(x,y,t)$ due to Parseval's identity.

For convenience in numerical simulation, we use an equivalent formula for $\Theta_V[f](x,k,t)$ given by

$$\Theta_V[f](x,k,t)=-\int_{-\infty}^{+\infty}V_w(x,k-k')f(x,k',t)\mathrm{d}k', \tag{2.6}$$

where the non-local Wigner potential $V_w(x,k)$ is calculated from the physical potential by a Fourier transform as

$$V_w(x,k)=\frac{1}{2\pi\mathrm{i}\hbar}\int_{-\infty}^{+\infty}\exp(-\mathrm{i}ky)D_V(x,y)\mathrm{d}y. \tag{2.7}$$

The Wigner function can be used to calculate the electron density $\mathrm{n}(x,t)$ by

$$\mathrm{n}(x,t)=\frac{1}{2\pi}\int_{-\infty}^{+\infty}f(x,k,t)\mathrm{d}k, \tag{2.8}$$

and the current density $\mathrm{j}(x,t)$ by

$$\mathrm{j}(x,t)=\frac{\hbar}{2\pi m}\int_{-\infty}^{+\infty}kf(x,k,t)\mathrm{d}k. \tag{2.9}$$

In addition, we denote the integration of the potential term with respect to k as

$$\mathrm{p}(x,t)=\frac{1}{2\pi}\int_{-\infty}^{+\infty}\mathrm{d}k\int_{-\infty}^{+\infty}\mathrm{d}k'V_w(x,k-k')f(x,k',t). \tag{2.10}$$

Due to the anti-symmetry of $V_w(x,k)$ in k, $\mathrm{p}(x,t)$ vanishes and we obtain a continuity equation for the electron,

$$\frac{\partial}{\partial t}\mathrm{n}(x,t)+\frac{\partial}{\partial x}\mathrm{j}(x,t)=-\mathrm{p}(x,t)=0. \tag{2.11}$$

This continuity equation corresponds to conservation of the zeroth moment, i.e., the mass conservation.

2.1 Wigner equation in the truncated phase space and mass conservation

For numerical computation of the Wigner equations in the phase space, boundary conditions in both the x and the k spaces will be needed to truncate the infinite phase space. For the x-space, the popular quantum transitive boundary condition (upwinding one-way wave conditions) by Frensley [9] can be easily applied. And, there are two ways to truncate the k-space. One is to use a periodic extension of the distribution function over a finite interval, which is the approach of plane wave expansion methods [21]. The plane wave turns out to be the eigen-function of the pseudo-differential operator (2.4) in the Wigner equation, thus greatly simplifying the calculation of the integral operator. The other approach, employed in this paper, will be a simple nullification of the distribution outside a sufficiently large k-domain $\mathcal{K}=[k_{\min},k_{\max}]$. The k-integration range in (2.8)-(2.10) for the electron density and fluxes will be then changed to $\mathcal{K}$. The size

$$|\mathcal{K}|=k_{\max}-k_{\min}$$

needed depends on the decay of the Wigner distribution for large wave number k and affects the accuracy of the numerical solutions. The distribution function will be represented in the k-space by Chebyshev polynomials (or piecewise Chebyshev polynomials if $\mathcal{K}$ is further sub-divided into elements for adaptivity, giving the Spectral Element Method in this paper).

Due to the decay of $\widehat{f}(x,y,t)$ as $|y|\to\infty$, we only need to consider $\widehat{f}(x,y,t)$ for $|y|\le 2Y$, for some large Y. As mentioned above, $f(x,k,t)$ is also usually significant or needed for $k\in\mathcal{K}$ (thus negligible for $k\notin\mathcal{K}$), therefore, (2.5) can be replaced by

$$\widehat{f}(x,y,t)\approx\frac{1}{2\pi}\int_{k_{\min}}^{k_{\max}}\exp(\mathrm{i}ky)f(x,k,t)\mathrm{d}k,\quad |y|<2Y. \tag{2.12}$$

In this case, $f(x,k,t)$ can be shown to satisfy a modified version of the Wigner equation (2.3) for $|x|<\infty$,

$$\frac{\partial}{\partial t}f(x,k,t)+\frac{\hbar k}{m}\frac{\partial}{\partial x}f(x,k,t)+\int_{k_{\min}}^{k_{\max}}V_w(x,k-k')f(x,k',t)\mathrm{d}k'=0,\quad |x|<\infty,\quad k\in\mathcal{K}, \tag{2.13}$$

where the Wigner potential $V_w(x,k)$ has been approximated as

$$\begin{aligned}V_w(x,k)&\approx\frac{1}{2\pi\mathrm{i}\hbar}\int_{-2Y}^{2Y}\exp(-\mathrm{i}ky)D_V(x,y)\mathrm{d}y\\&=\frac{2}{\pi\hbar}\int_0^Y\sin(2ky)\big[V(x+y)-V(x-y)\big]\mathrm{d}y.\end{aligned} \tag{2.14}$$

In actual simulations, we should make sure that the truncation length Y is large enough. For potentials of compact supports or of exponential decays such as Gauss-type potential $V(x)$, there is a simple way to choose Y as shown later.

An important issue of using the SEM with a non-uniform mesh in the k-space is to ensure the mass conservation of electrons for the numerical solution. As pointed out in [17], conservation of mass is the most important property that a discretization of the Wigner equation should fulfill.

First of all, the Wigner potential $V_w(x,k)$ has to be replaced by a discretized version, say, using a trapezoid rule with a spacing Δy as follows

$$V_w(x,k)\approx V_w^h(x,k):=\frac{2\Delta y}{\pi\hbar}\sum_{\mu=1}^{N_y}\sin(2ky_\mu)\left[V(x+y_\mu)-V(x-y_\mu)\right], \tag{2.15a}$$

where

$$N_y\Delta y=Y, \qquad y_\mu=\mu\Delta y, \qquad \mu=1,\cdots,N_y. \tag{2.15b}$$

In order to keep the mass conservation, we require

$$\int_{\mathcal{K}}\mathrm{d}k\int_{\mathcal{K}}\mathrm{d}k' V_w^h(x,k-k')f(x,k',t)=0, \tag{2.16}$$

for $V_w^h(x,k)$ with $k\in\mathcal{K}$. Frensley suggested in [8,9] a sufficient condition

$$|\mathcal{K}|\Delta y=\pi, \tag{2.17}$$

which guarantees that $V_w^h(x,k)$ is not only odd but also periodic in k with a period $|\mathcal{K}|$. (2.16) can be easily verified by noting that, with the condition (2.17),

$$\begin{aligned}\int_{\mathcal{K}}\sin\left[2(k-k')y_\mu\right]\mathrm{d}k&=\frac{\cos\left[2y_\mu(k_{\min}-k')\right]-\cos\left[2y_\mu(k_{\max}-k')\right]}{2y_\mu}\\&=\frac{\cos[2\mu\Delta y(k_{\min}-k')]-\cos[2\mu\Delta y(k_{\min}-k')+2\mu\Delta y|\mathcal{K}|]}{2\mu\Delta y}=0.\end{aligned} \tag{2.18}$$

Remark 2.1. It is pointed out in [17] that the condition (2.17) will result in a "constraint" on the size of the domain $\mathcal{K}$, while using uniform FDMs to solve the Wigner equation. (2.17) says that the length of the computational domain $\mathcal{K}$ in the k-space should be doubled after halving the y-mesh size. If we use the same spacing in the x-space and the y-space, then we need four times as many grid points in the k-space and twice as many grid points in the x-space to double the resolution of $f(x,k,t)$. This results in huge cost for high-dimensional cases.

To sum up, we have truncated the infinite domains in (2.6) and (2.7) and adopted the trapezoid rule for the y-integration of the Wigner potential $V_w(x,k)$ in (2.14). Next, we will present our adaptive conservative SEM for

$$\frac{\partial}{\partial t}f(x,k,t)+\frac{\hbar k}{m}\frac{\partial}{\partial x}f(x,k,t)+\int_{\mathcal{K}}V_w^h(x,k-k')f(x,k',t)\mathrm{d}k'=0, \quad (x,k)\in\mathcal{X}\times\mathcal{K}, \tag{2.19}$$

where $\mathcal{X}$ is the computational domain in the x-space.

2.2 Boundary and initial conditions

The Wigner equation only contains a first-order spatial x-derivative, which means that we need to specify only one boundary condition in the x-space. In the following, we will use the inflow boundary conditions [8]

$$\begin{aligned} f(x_{\min},k,t) &= f_L(k,t), \qquad \text{if} \quad k>0, \\ f(x_{\max},k,t) &= f_R(k,t), \qquad \text{if} \quad k<0. \end{aligned}$$

Also, the initial condition is given as

$$f(x,k,t=0)=f_0(x,k), \qquad (x,k)\in\mathcal{X}\times\mathcal{K}. \tag{2.20}$$

3 Numerical schemes

In this section, we present the conservative cell average SEM in the k-space with Gauss-Chebyshev collocation points, the traditional SEM in the x-space with Gauss-Lobatto collocation points and a time discretization with multi-step Runge-Kutta methods. The cell average SEM in the k-space will allow us to maintain strict electron conservation of the numerical solution using the fact that there is an analytical relation between the k-cell averages and the k-point values of the Wigner distribution function represented by the Chebyshev polynomials of the k-variable. The resulting SEM in the k-space will keep discrete mass conservation analytically even with a non-uniform mesh, leading to conservative adaptive solutions in the phase space of high dimensions.

The computational domain $\mathcal{X}\times\mathcal{K}$ is divided into $Q\times R$ non-overlapping elements (sub-domains) as

$$\mathcal{X}\times\mathcal{K}=\bigcup_{q=1}^{Q}\bigcup_{r=1}^{R}\mathcal{X}_q\times\mathcal{K}_r, \qquad \mathcal{X}_q=[g_{q-1},g_q], \qquad \mathcal{K}_r=[d_{r-1},d_r],$$

with

$$g_0=x_{\min}, \qquad g_Q=x_{\max}, \qquad d_0=k_{\min}, \qquad d_R=k_{\max}.$$

In an element $\mathcal{X}_q\times\mathcal{K}_r$ ($q=1,\cdots,Q$ and $r=1,\cdots,R$), the collocation points are $\{(x_{i;q,r},k_{j;q,r})\}$ with $i=0,1,\cdots,M_{q,r}$ and $j=1,\cdots,N_{q,r}$, so we have $(M_{q,r}+1)\times N_{q,r}$ collocation points. Here, we set $x_{i;q,r}$ to be Gauss-Lobatto points and $k_{j;q,r}$ to be Gauss-Chebyshev points to take advantage of the fast Fourier transforms [32]

$$\text{(Gauss-Lobatto)} \qquad x_{i;q,r}=g_{q-1}+\frac{G_q}{2}\left(1+\cos\frac{i\pi}{M_{q,r}}\right), \tag{3.1a}$$

$$\text{(Gauss-Chebyshev)} \qquad k_{j;q,r}=d_{r-1}+\frac{D_r}{2}\left[1+\cos\left(j-\frac{1}{2}\right)\frac{\pi}{N_{q,r}}\right], \tag{3.1b}$$

where

$$G_q = g_q - g_{q-1} \quad \text{and} \quad D_r = d_r - d_{r-1}.$$

Denote by $f_{q,r}(x,k,t)$ the restriction of the Wigner function $f(x,k,t)$ on the element $\mathcal{X}_q \times \mathcal{K}_r$ and $f_{j,i;q,r}(t) := f_{q,r}(x_{i;q,r}, k_{j;q,r}, t)$.

A uniform mesh means choosing the same $(M_{q,r}, N_{q,r})$ for all q and r, i.e., $M_{q,r}$ and $N_{q,r}$ are two constants, while the non-uniform mesh allows different $(M_{q,r}, N_{q,r})$ in different elements. The total number of unknowns is denoted by $\mathcal{N}$

$$\mathcal{N} = \sum_{q=1}^{Q} \sum_{r=1}^{R} (M_{q,r}+1) \times N_{q,r}. \tag{3.2}$$

In the rest of this section, we will take the element $\mathcal{X}_q \times \mathcal{K}_r$ as an example to illustrate the adaptive conservative cell average SEM and the subscripts q and r for the (q,r)-element under consideration will be dropped from $x_{i;q,r}$, $k_{j;q,r}$, $M_{q,r}$, $N_{q,r}$, $f_{q,r}(x,k,t)$, $f_{j,i;q,r}(t)$.

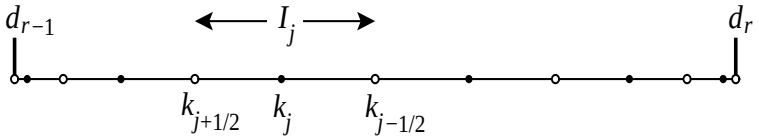

Figure 1: k-mesh in the sub-domain $\mathcal{K}_r = [d_{r-1}, d_r]$. The black points are Gauss-Chebyshev collocation points, denoted by k_j. The ends of cells are $k_{j\mp 1/2}$ displayed in small circles.

3.1 Cell average spectral element method in the k-space

A cell I_j in the k-space is given as (see Fig. 1) $I_j = \left[k_{j+\frac{1}{2}}, k_{j-\frac{1}{2}}\right]$, with

$$k_{j\mp\frac{1}{2}} = d_{r-1} + \frac{D_r}{2}\left[1+\cos\left(j-\frac{1}{2}\mp\frac{1}{2}\right)\frac{\pi}{N}\right].$$

Obviously, we have

$$\mathcal{K}_r = \bigcup_{j=1}^{N} I_j.$$

We define local quantities corresponding to $\mathrm{n}(x,t)$, $\mathrm{j}(x,t)$ and $\mathrm{p}(x,t)$ in each computational cell as follows

$$\mathrm{n}_j(x,t) := \frac{1}{2\pi}\int_{I_j} f(x,k,t)\mathrm{d}k, \tag{3.3a}$$

$$\mathrm{j}_j(x,t) := \frac{\hbar}{2\pi m}\int_{I_j} k f(x,k,t)\mathrm{d}k, \tag{3.3b}$$

$$\mathrm{p}_j(x,t) := \frac{1}{2\pi}\int_{I_j}\int_{\mathcal{K}} V_w^h(x,k-k')f(x,k',t)\mathrm{d}k'\mathrm{d}k. \tag{3.3c}$$

Then, a local continuity equation for the cell I_j is defined as

$$\frac{\partial}{\partial t}\mathrm{n}_j(x,t)+\frac{\partial}{\partial x}\mathrm{j}_j(x,t)+\mathrm{p}_j(x,t)=0. \tag{3.4}$$

From (3.3a)-(3.3c), we can see that both cell averages and point values of the Wigner function $f(x,k,t)$, expressed in terms of the Chebyshev polynomials of the k-variable over each cell, are involved in (3.4). Fortunately, in the Chebyshev polynomial space, there is an analytical relation between the expansions for $\mathrm{n}_j(x,t)$, $\mathrm{j}_j(x,t)$ and $\mathrm{p}_j(x,t)$ as shown below.

For $k\in\mathcal{K}_r$, $\eta\in[-1,1]$ and $\theta\in[0,\pi]$, we use the following transform:

$$k=d_{r-1}+\frac{D_r}{2}(1+\eta),\qquad \eta=\cos\theta,$$

to define

$$C_l(k)=T_l(\eta)=\cos l\theta,\qquad S_l(k)=\sin(l+1)\theta, \tag{3.5}$$

with $l=0,1,\cdots,N-1$, where $T_l(\eta)$ is the Chebyshev polynomial of the first kind. Then, we have a spectral approximation

$$f(x,k,t)\approx\widetilde{f}(x,k,t):=\sum_{l=0}^{N-1}a_l(x,t)C_l(k),\quad k\in\mathcal{K}_r. \tag{3.6}$$

Consequently, plugging the approximation for the Wigner function into (3.3a)-(3.3c), we have spectral approximations for n_j, j_j and p_j, which are denoted by $\tilde{\mathrm{n}}_j$, $\widetilde{\mathrm{j}}_j$ and $\widetilde{\mathrm{p}}_j$, respectively.

We proceed by substituting the above expansion (3.6) into (3.3a) and (3.3b) and using the following two identities for θ, $\theta\pm\Delta\theta/2\in[0,\pi]$:

$$\int_{\cos(\theta-\Delta\theta/2)}^{\cos(\theta+\Delta\theta/2)}\mathrm{d}\eta T_l(\eta)=\begin{cases}-\dfrac{\sin\Delta\theta}{2}\sin2\theta, & l=1,\\ \dfrac{\sin[(l-1)\Delta\theta/2]}{l-1}\sin(l-1)\theta-\dfrac{\sin[(l+1)\Delta\theta/2]}{l+1}\sin(l+1)\theta, & l\neq1,\end{cases}$$

$$\int_{\cos(\theta-\Delta\theta/2)}^{\cos(\theta+\Delta\theta/2)}\mathrm{d}\eta\eta T_l(\eta)=\begin{cases}-\dfrac{\sin2\Delta\theta}{8}\sin4\theta, & l=2,\\ \dfrac{\sin[(l-2)\Delta\theta/2]}{2(l-2)}\sin(l-2)\theta-\dfrac{\sin[(l+2)\Delta\theta/2]}{2(l+2)}\sin(l+2)\theta, & l\neq2,\end{cases}$$

and Eqs. (3.3a), (3.3b) and (3.5), obtain

$$\mathrm{n}_j(x,t)\approx\tilde{\mathrm{n}}_j(x,t):=\frac{1}{2\pi}\sum_{l=0}^{N-1}a_l(x,t)\Big[\int_{I_j}C_l(k)\mathrm{d}k\Big]=-\frac{1}{2\pi}\sum_{l=0}^{N-1}b_l(x,t)S_l(k_j), \tag{3.7a}$$

$$\mathrm{j}_j(x,t)\approx\widetilde{\mathrm{j}}_j(x,t):=\frac{\hbar}{2\pi m}\sum_{l=0}^{N-1}a_l(x,t)\Big[\int_{I_j}kC_l(k)\mathrm{d}k\Big]=-\frac{\hbar}{2m\pi}\sum_{l=0}^{N}c_l(x,t)S_l(k_j). \tag{3.7b}$$

Here, the expansion coefficients b_l and c_l can be expressed in terms of a_l recursively as follows:

$$b_l=\begin{cases}\sigma_0(a_2-2a_0), & l=0,\\ \sigma_l(a_{l+2}-a_l), & l=1,\cdots,N-3,\\ -\sigma_l a_l, & l=N-2,N-1,\end{cases}\qquad a_l=\begin{cases}-b_l/\sigma_l, & l=N-1,N-2,\\ a_{l+2}-b_l/\sigma_l, & l=N-3,\cdots,1,\\ \frac{1}{2}(a_2-b_0/\sigma_0), & l=0,\end{cases}\tag{3.8a}$$

$$c_l=\begin{cases}\bar{d}_r b_0+\dfrac{D_r\sigma_0}{4}(a_3-a_1), & l=0,\\ \bar{d}_r b_1+\dfrac{D_r\sigma_1}{4}(a_4-2a_0), & l=1,\\ \bar{d}_r b_l+\dfrac{D_r\sigma_l}{4}(a_{l+3}-a_{l-1}), & l=2,3,\cdots,N-4,\\ \bar{d}_r b_l-\dfrac{D_r\sigma_l}{4}a_{l-1}, & l=N-3,N-2,N-1,\\ -\dfrac{D_r\sigma_N}{4}a_{N-1}, & l=N,\end{cases}\tag{3.8b}$$

where $\bar{d}_r$ denotes the center of $\mathcal{K}_r$ and

$$\sigma_l=\frac{D_r\sin[(l+1)\pi/2N]}{2(l+1)},\qquad l=0,1,\cdots,N.\tag{3.9}$$

It is easily seen that we can transform $b_l(x,t)$ to $\widetilde{\mathrm{n}}_j(x,t)$ in (3.7a) via a fast sine transform (FST) and $c_l(x,t)$ to $\widetilde{\mathrm{j}}_j(x,t)$ in (3.7b) via another FST.

Meanwhile, substituting (3.6) into (3.3c) and through some careful algebraic calculation, we can show that

$$\mathrm{p}_j(x,t)\approx\widetilde{\mathrm{p}}_j(x,t),$$

with

$$\begin{aligned}\widetilde{\mathrm{p}}_j(x,t):=&\frac{\Delta y}{\pi^2\hbar}\sum_{\mu=1}^{N_y}[V(x+y_\mu)-V(x-y_\mu)]\sum_{r'=1}^{R}\int_{\mathcal{K}_{r'}}\mathrm{d}k'\\ &\times\Big\{\int_{I_j}\sin[2y_\mu(k-k')]\mathrm{d}k\Big\}\sum_{l=0}^{N_{q,r'}-1}a_{l;q,r'}(x,t)C_{l;q,r'}(k')\\ =&-\frac{\Delta y}{\pi^2\hbar}\sum_{\mu=1}^{N_y}\sin(y_\mu\Delta k_j)\chi(x,y_\mu)\sum_{r'=1}^{R}D_{r'}\times\Big\{\sin[2y_\mu(\bar{k}_j-\bar{d}_{r'})]\mathrm{Re}[\lambda(x,y_\mu,t,r')]\\ &-\cos[2y_\mu(\bar{k}_j-\bar{d}_{r'})]\mathrm{Im}[\lambda(x,y_\mu,t,r')]\Big\},\end{aligned}\tag{3.10}$$

where

$$\chi(x,y_\mu):=\frac{V(x+y_\mu)-V(x-y_\mu)}{2y_\mu},\tag{3.11a}$$

$$\lambda(x,y,t,r'):=\sum_{l=0}^{N_{q,r'}-1}a_{l;q,r'}(x,t)O_l(D_{r'}y),\tag{3.11b}$$

$\bar{k}_j$ is the middle point of the cell I_j and we have used the spectral expansion in the element $\mathcal{X}_q \times \mathcal{K}_{r'}$, i.e.,

$$f_{q,r'}(x,k,t) \approx \sum_{l=0}^{N_{q,r'}-1} a_{l;q,r'}(x,t) C_{l;q,r'}(k).$$

Here r' comes from the integral with respect to k' in the sub-domain $\mathcal{K}_{r'}$, $\Delta k_j = k_{j-1/2} - k_{j+1/2}$ and $O_l(z)$ is an oscillatory integral given in (A.1) of the Appendix, where an analytical calculation is given.

In order to determine the expansion coefficients a_l in (3.6), we solve the approximated local continuity equation

$$\frac{\partial}{\partial t}\widetilde{\mathrm{n}}_j(x,t) + \frac{\partial}{\partial x}\widetilde{\mathrm{j}}_j(x,t) + \widetilde{\mathrm{p}}_j(x,t) = 0, \tag{3.12}$$

with the spectral approximations (3.7a), (3.7b) and (3.10). It is noted that there are only spectral errors associated with the Chebyshev polynomial expansion of $f(x,k,t)$ in (3.6), since all the integrals in (3.3a), (3.3b) and (3.3c) are calculated analytically.

Remark 3.1. (Exact Mass Conservation) The cell equation (3.12) involves the cell averages of the Wigner function, the cell fluxes involving the point values of $f(x,k,t)$ over the whole cell and the local Wigner potential term p_j involving $f(x,k,t)$ and the Wigner potential, where all integrals are carried out exactly. If our primary unknowns are selected to be the cell averages $\widetilde{\mathrm{n}}_j(x,t)$, such an exact calculation is only possible if the distribution function $f(x,k,t)$ is represented by a global (Chebyshev) polynomial in the domain $\mathcal{K}_r$ due to the analytical relation between the cell averages of $\widetilde{f}(x,k,t)$ ($\widetilde{\mathrm{n}}_j(x,t)$) and the point values without numerical errors. As a result, we can sum all cell equations for the $\widetilde{f}(x,k,t)$ and the summation of $\widetilde{\mathrm{p}}_j(x,t)$ for all elements will be zero, i.e.,

$$\Theta(x,t) := \sum_{r=1}^{R}\sum_{j=1}^{N_{q,r}} \widetilde{\mathrm{p}}_{j;q,r}(x,t) = \int_{\mathcal{K}} \mathrm{d}k \int_{\mathcal{K}} \mathrm{d}k' V_w^h(x,k-k')\widetilde{f}(x,k',t) = 0, \qquad \forall x \in \mathcal{X}, \tag{3.13}$$

thanks to (2.18). Therefore, we can see that the proposed cell average SEM is capable of maintaining the mass conservation exactly for the spectral solution $\widetilde{f}(x,k,t)$ in a non-uniform mesh.

3.2 Spectral element method in the x-space

After forming the above conservative cell average SEM in the k-space, we will solve the local continuity equation (3.12) to get the expansion coefficients in (3.6) by using a traditional collocation SEM with Gauss-Lobatto points in the x-space for easy implementation of boundary conditions and fast cosine transforms.

For $x\in\mathcal{X}_q$, $\eta\in[-1,1]$ and $\theta\in[0,\pi]$, the transform

$$x=g_{q-1}+\frac{G_q}{2}(1+\eta),\qquad \eta=\cos\theta,$$

is used to define

$$\phi_\nu(x)=T_\nu(\eta)=\cos\nu\theta,\qquad \nu=0,1,\cdots,M. \tag{3.14}$$

Then, we have the spectral expansion for the coefficients in (3.6) as

$$a_l(x,t)\approx\sum_{\nu=0}^{M}\beta_{l,\nu}(t)\phi_\nu(x),\qquad x\in\mathcal{X}_q, \tag{3.15}$$

where $\beta_{l,\nu}$ are the expansion coefficients. Based on such an expansion, we can obtain the first derivative by a recurrence [32,33] with $\mathcal{O}(M)$ operations. Namely, if a function is expressed in terms of the Chebyshev polynomials, then, its first derivative can be obtained directly as

$$\frac{\partial a_l(x,t)}{\partial x}\approx\sum_{\nu=0}^{M}\widetilde{\beta}_{l,\nu}(t)\phi_\nu(x),\qquad x\in\mathcal{X}_q, \tag{3.16}$$

where

$$\widetilde{\beta}_{l,\nu}(t)=\frac{2}{G_q}\times\begin{cases}0, & \nu=M,\\ 2M\beta_{l,M}(t), & \nu=M-1,\\ \widetilde{\beta}_{l,\nu+2}(t)+2(\nu+1)\beta_{l,\nu+1}(t), & \nu=M-2,\cdots,1,\\ \frac{1}{2}\widetilde{\beta}_{l,2}(t)+\beta_{l,1}(t), & \nu=0.\end{cases} \tag{3.17}$$

Hence, we could obtain the convection term via a fast cosine transform (FCT) and a recurrence and the total cost is $\mathcal{O}(M\log M)$.

3.3 Time discretization

For the time discretization, we employ explicit multi-step Runge-Kutta methods. If a system of the ODEs is given in a compact operator form

$$\frac{\mathrm{d}}{\mathrm{d}t}U(t)=L(U), \tag{3.18}$$

then, the fourth-order Runge-Kutta scheme is given as [29]

$$U^{(1)}=U^n+\frac{1}{2}\Delta tL(U^n), \tag{3.19a}$$

$$U^{(2)}=U^n+\frac{1}{2}\Delta tL(U^{(1)}), \tag{3.19b}$$

$$U^{(3)}=U^n+\Delta tL(U^{(2)}), \tag{3.19c}$$

$$U^{n+1}=\frac{1}{3}\Big[U^{(1)}+2U^{(2)}+U^{(3)}-U^n+\frac{1}{2}\Delta tL(U^{(3)})\Big]. \tag{3.19d}$$

Let

$$t^n = n\Delta t, \quad n = 0,1,\cdots, \quad \text{and} \quad f^n_{j,i} := f_{j,i}(t^n).$$

The time step Δt is restricted by the Courant-Friedrichs-Levy (CFL) condition as

$$\frac{\Delta t}{\min_i\{\Delta x_i\}} \le \frac{m}{\hbar \max_{k\in\mathcal{K}}\{|k|\}}, \tag{3.20}$$

where $\Delta x_i = |x_{i+1} - x_i|$. After discretization in both the k-space and the x-space, we have the spectral element approximation at time step t^n,

$$f^n_{j,i} \approx \widetilde{f}^n_{j,i} = \sum_{l=0}^{N-1} a^n_{l,i} C_l(k_j) = \sum_{l=0}^{N-1}\sum_{\nu=0}^{M} \beta^n_{l,\nu}\phi_\nu(x_i)C_l(k_j). \tag{3.21}$$

Once the coefficients $\beta^n_{l,\nu}$ are obtained, we are able to compute the Wigner function at any position (x,k) in the element $\mathcal{X}_q \times \mathcal{K}_r$ at t^n through the global spectral approximation

$$f(x,k,t_n) \approx \sum_{l=0}^{N-1}\sum_{\nu=0}^{M} \beta^n_{l,\nu}\phi_\nu(x)C_l(k). \tag{3.22}$$

When evolving from t^n to t^{n+1}, we need boundary conditions in $\mathcal{X}_q \times \mathcal{K}_r$. These boundary conditions are given according to the inflow rule, from the solution in the adjacent elements at t^n, i.e.,

(a) if $k < 0$, then

$$f_{q,r}(g_q,k,t^{n+1}) = \begin{cases} f_{q+1,r}(g_q,k,t^n), & 1 \le q < Q, \\ f_R(k,t^n), & q = Q, \end{cases} \tag{3.23}$$

(b) if $k > 0$, then

$$f_{q,r}(g_{q-1},k,t^{n+1}) = \begin{cases} f_{q-1,r}(g_{q-1},k,t^n), & 1 < q \le Q, \\ f_L(k,t^n), & q = 1. \end{cases} \tag{3.24}$$

Here, we set $k = 0$ to be the end point of an element, so $k = 0$ is not a collocation point.

By using the special collocation points given in (3.1a) and (3.1b), we are able to take the full advantage of FST and FCT to improve the computational efficiency [32]. The related relations are shown in Fig. 2 and the cost is listed as follows:

(a) $a^n_{l,i} \Leftrightarrow f^n_{j,i}$: $\mathcal{O}(MN\log N)$,

(b) $a^n_{l,i} \Leftrightarrow \mathrm{n}^n_{j,i}$ and $a^n_{l,i} \Rightarrow \mathrm{j}^n_{j,i}$: $\mathcal{O}(MN\log N)$,

(c) $a^n_{l,i} \Rightarrow \frac{\partial}{\partial x} a^n_{l,i}$: $\mathcal{O}(NM\log M)$,

(d) $a^n_{l,i} \Rightarrow \mathrm{p}^n_{j,i}$: $\mathcal{O}(N_y M N_k)$,

(e) $a^n_{l,i} \Rightarrow \frac{\partial}{\partial x}\mathrm{j}^n_{j,i}$: $\mathcal{O}(NM\log M) + \mathcal{O}(MN\log N)$.

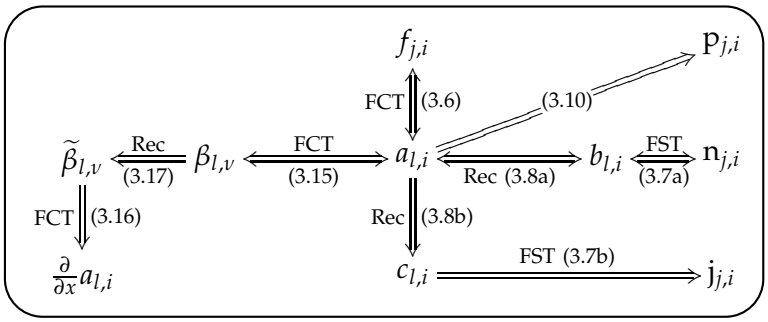

Figure 2: The transformation relation graph in the element $\mathcal{X}_q \times \mathcal{K}_r$. "FCT" denotes the fast cosine transform while "FST" the fast sine transform. "Rec" is the abbreviation of recurrence and "$\Leftrightarrow$" represents the reversible transform. Here, the recurrence needs $\mathcal{O}(\mathcal{S})$ operations and $\mathcal{O}(\mathcal{S}\log\mathcal{S})$ for FCT or FST, where $\mathcal{S}$ is the size of the sequence to be transformed.

Here, N_y and N_k are the number of total mesh points in the y-space and the k-space, respectively. In practice, the summation with respect to μ in (3.10) can be reduced by a large amount for localized potentials, for example, the Gaussian barrier shown in Fig. 6. The detailed discussion on this issue can be found in Section 4, where we will exploit further the local support property to find a way to determine the truncation domain in the y-space.

In our simulations, we use related subroutines in FFTPACK [34], i.e., COST, SINQF/SINQB, COSQF/COSQB, to implement FCT and FST mentioned above. And the calculation of the spherical Bessel functions of the first kind in (3.11b) and (A.8) is done with the subroutine BESSJY in [33].

3.4 p-adaptive methods

As shown in (3.21), we approximated the Wigner function in the element $\mathcal{X}_q \times \mathcal{K}_r$ with a spectral expansion. Generally, if the approximated function is smooth enough, we could expect its spectral approximation to have spectral convergence, i.e., the expansion coefficients decay exponentially to zero as the expansion order increases [32]. This forms the mathematical foundation for developing p-adaptive SEMs. In the following, we delineate the p-adaptive method for a given tolerance ϵ_T.

Assuming that we have known the solution $f_{j,i}^n$ with the expansion order $(\check{M}^n, \check{N}^n)$, according to the spectral expansion (3.21), we then obtain the coefficients $\beta_{l,\nu}^n$ through FCTs and denote

$$u_\nu^n = \max_{0\le l\le \check{N}^n-1} |\beta_{l,\nu}^n|, \qquad v_l^n = \max_{0\le \nu\le \check{M}^n} |\beta_{l,\nu}^n|. \tag{3.25}$$

Next, we examine u_ν^n in a reversed order, i.e., from $\nu = \check{M}^n$ to 0 and record the first index $\hat{M}^n$, such that $u_{\hat{M}^n-1}^n > \epsilon_T$ and $u_{\hat{M}^n}^n \le \epsilon_T$. Similarly, we can also get $\hat{N}^n$ by examining v_l^n. The mesh associated with the expansion order $(\hat{M}^n, \hat{N}^n)$ in the element $\mathcal{X}_q \times \mathcal{K}_r$ has the minimal size among those satisfying the accuracy tolerance ϵ_T at the time t^n.

The p-adaptive method introduces an index buffer, the size of which could be dynamically adjusted by a restarting strategy. As we have shown in the element $\mathcal{X}_q \times \mathcal{K}_r$, the minimal expansion order for satisfying the prescribed accuracy tolerance ϵ_T at the time t^n is $(\hat{M}^n, \hat{N}^n)$. In actual adaptive calculations, we will adjust dynamically the expansion order to maintain the accuracy. For example, if the expansion order happens to increase from t^n to t^{n+1}, i.e., $\hat{M}^{n+1} > \hat{M}^n$, then we should reserve an index buffer at t^n for a possible longer expansion in the x-space at t^{n+1}. Denoting by A^n the buffer size for the Chebyshev expansion in the x-space and by B^n the buffer size for the Chebyshev expansion in the k-space, we have the expansion orders at the time step t^{n+1} as

$$\check{M}^{n+1} = \hat{M}^n + A^n, \qquad \check{N}^{n+1} = \hat{N}^n + B^n. \tag{3.26}$$

Here, $(\hat{M}^n, \hat{N}^n)$ is obtained by examining $\beta^n_{l,\nu}$ as before for $l = 0,1,\cdots,\check{N}^n - 1$ and $\nu = 0,1,\cdots,\check{M}^n$.

The buffer size (A^n, B^n) is dynamically adjusted through the following restarting procedure. Intuitively, we are able to judge whether the buffer size should be adjusted through examining $u^n_{\check{M}^n}$ or $v^n_{\check{N}^n}$ with ϵ_T. If $u^n_{\check{M}^n} > \epsilon_T$, the buffer is not large enough to maintain accuracy at the instant t^n in the x-space, then, we should restart the computation from an earlier time t^{n_0} with a larger buffer size A^{n_0}: $A^{n_0} = A^n + 1$; otherwise $A^n = A^{n-1}$. B^n is updated in a similar way by considering whether $v^n_{\check{N}^n} > \epsilon_T$ holds. To implement this strategy, we set

$$n_0 = \alpha_{Z_0}(n), \tag{3.27}$$

where Z_0 is a prescribed largest backward restarting time step and the function $\alpha_{Z_0}(n)$ is defined by

$$\alpha_{Z_0}(n) = \begin{cases} n - Z_0, & \text{if} \quad \mathrm{MOD}(n, Z_0) = 0, \\ n - \mathrm{MOD}(n, Z_0), & \text{if} \quad \mathrm{MOD}(n, Z_0) \neq 0, \end{cases} \tag{3.28}$$

with $\mathrm{MOD}(n, Z_0)$ giving the remainder of n divided by Z_0. For example, we have $n_0 = n - 1$ if taking $Z_0 = 1$, which means that we need to restart from the previous step. The total size of collocation points at t^n is $\check{\mathcal{N}}^n$ given in (3.2). Once the mesh for the $(n+1)$-th time step, i.e., $\{\check{M}^{n+1}, \check{N}^{n+1}\}$, is known, we march time from $f^n_{j,i}$ to $f^{n+1}_{j,i}$ in the new mesh after $f^n_{j,i}$ on the mesh $\{\check{M}^n, \check{N}^n\}$ is interpolated into $\check{f}^n_{j,i}$ over the $(n+1)$-th time step new mesh. The interpolation is straightforward as the spectral approximation

$$f(x,k,t_n) \approx \sum_{l=0}^{\check{N}^n - 1} \sum_{\nu=0}^{\check{M}^n} \beta^n_{l,\nu} \phi_\nu(x) C_l(k),$$

is global within the element $\mathcal{X}_q \times \mathcal{K}_r$. The flowchart of the restarting p-adaptive method is shown in Fig. 3.

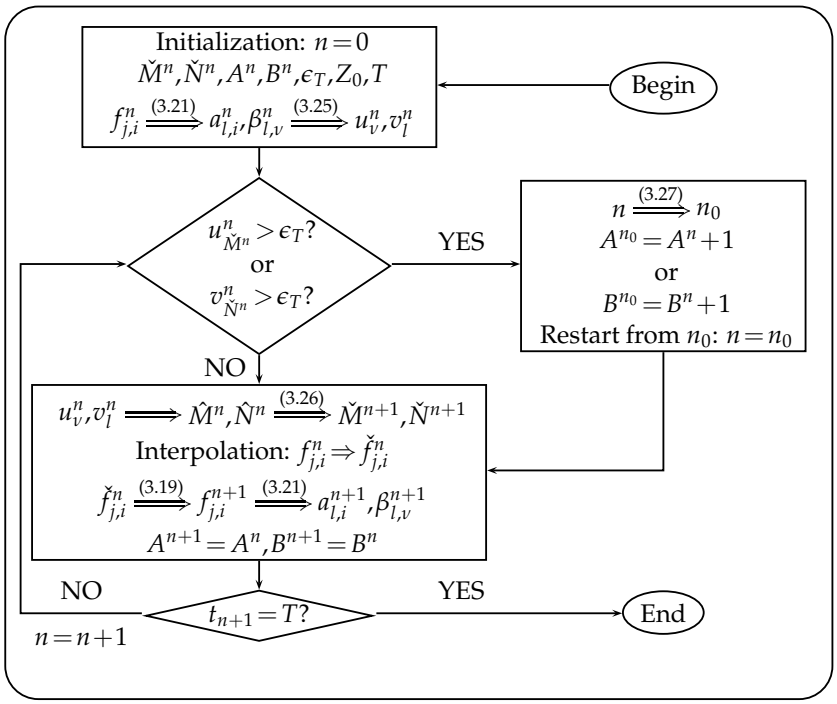

Figure 3: The flowchart of p-adaptive methods in the element $\mathcal{X}_q \times \mathcal{K}_r$.

4 Numerical results

The physical units and quantities in our numerical experiments are listed in Table 1. Following [11, 14, 35], we simulate the motion of a Gauss wave packet (GWP) to investigate the performance of the proposed SEM. The GWP in the free space is

$$f(x,k,t) = 2\exp\Big[-\frac{(x-x_0-v_0t)^2}{2a^2(1+\beta^2t^2)}\Big]\cdot\exp\Big\{-2a^2(1+\beta^2t^2)\Big[(k-k_0)-\frac{\beta t(x-x_0-v_0t)}{2a^2(1+\beta^2t^2)}\Big]^2\Big\}, \tag{4.1}$$

where x_0 is the center of the GWP at $t=0$, a is the minimum position spread, $v_0=\hbar k_0/m$ is the average velocity and $\beta=\hbar/2ma^2$. The kinetic energy of such a GWP is $E_0=\hbar^2k_0^2/2m$. Actually, the GWP (4.1) is the analytical solution to the Wigner equation without a Wigner potential [11, 12]. In our numerical simulations, we take $a=2.825$ and $m=0.0665m_e$.

We employ the L^2 error and the L^∞ error to study the convergence rate of our algorithm. Let $f^{\rm ref}(x,k,t)$ denote the reference solution which could be the exact solution or the numerical solution on a relatively fine mesh and $f^{\rm num}(x,k,t)$ the numerical solution.

Table 1: Units and parameters.

Meaning	Unit	Value
Time	femtosecond (fs)	–
Length	nanometer (nm)	–
Energy	electron volt (eV)	–
Temperature	Kelvin (K)	–
Electron mass m_e	$\mathrm{eV\cdot fs^2\cdot nm^{-2}}$	5.68562966
Planck constant $\hbar$	$\mathrm{eV\cdot fs}$	0.658211899
Boltzmann constant k_B	$\mathrm{eV\cdot K^{-1}}$	8.61734279×10^{-5}

Then, the errors at a given time are written as

$$\varepsilon_2 = \Big[\int_{\mathcal{X}\times\mathcal{K}} \big(\Delta f(x,k)\big)^2 \mathrm{d}x\mathrm{d}k\Big]^{\frac{1}{2}}, \tag{4.2a}$$

$$\varepsilon_\infty = \max_{(x,k)\in\mathcal{X}\times\mathcal{K}} \Delta f(x,k), \tag{4.2b}$$

where

$$\Delta f(x,k,t) = |f^{\mathrm{num}}(x,k,t) - f^{\mathrm{ref}}(x,k,t)|,$$

and the integrals above are evaluated using a simple rectangular rule over a uniform mesh,

$$x_i = x_{\min} + \Big(i-\frac{1}{2}\Big) * h_x, \qquad k_j = k_{\min} + \Big(j-\frac{1}{2}\Big) * h_k,$$

with $i=1,2,\cdots,200$, $j=1,2,\cdots,400$, where

$$h_x = \frac{x_{\max}-x_{\min}}{200} \quad \text{and} \quad h_k = \frac{k_{\max}-k_{\min}}{400}.$$

In the following experiments, we set the final time $T=20$ to calculate the errors. Two kinds of meshes are used.

(a) A uniform mesh: the expansion order $\{M_{q,r},N_{q,r}\}$; the total size $\mathcal{N}$.

(b) An adaptive mesh: the expansion order $\{\check{M}^n_{q,r},\check{N}^n_{q,r}\}$, $\check{M}_{\max}:=\max_{q,r,n}\check{M}^n_{q,r}$, $\check{N}_{\max}:=\max_{q,r,n}\check{N}^n_{q,r}$; the buffer size $\{A^n_{q,r},B^n_{q,r}\}$, $A_{\max}:=\max_{q,r,n}A^n_{q,r}$, $B_{\max}:=\max_{q,r,n}B^n_{q,r}$; the total size $\check{\mathcal{N}}^n$, $\check{\mathcal{N}}_{\max}:=\max_n\check{\mathcal{N}}^n$; the ratio $\check{\mathcal{N}}_{\max}/\mathcal{N}^{\mathrm{ref}}$, where $\mathcal{N}^{\mathrm{ref}}$ is the size of the uniform mesh for the reference solution.

Example 4.1. In order to test the accuracy, we consider three cases given in Table 5.1 of [11], where GWP is the exact solution to the Wigner equation with $V\equiv0$, i.e., in the free space. We take the parameters: $x_{\min}=-30$, $x_{\max}=30$, $k_{\min}=-2.8$, $k_{\max}=2.8$, $R=Q=10$, $N_{q,r}=M_{q,r}\equiv N$, for $r=1,\cdots,R$, $q=1,\cdots,Q$. In Table 5.1 of [11], three different initial setups are considered: $x_0=0$ and $k_0=0$ for Case I; $x_0=-15$ and $k_0=0.7$ for Case II; $x_0=-30$

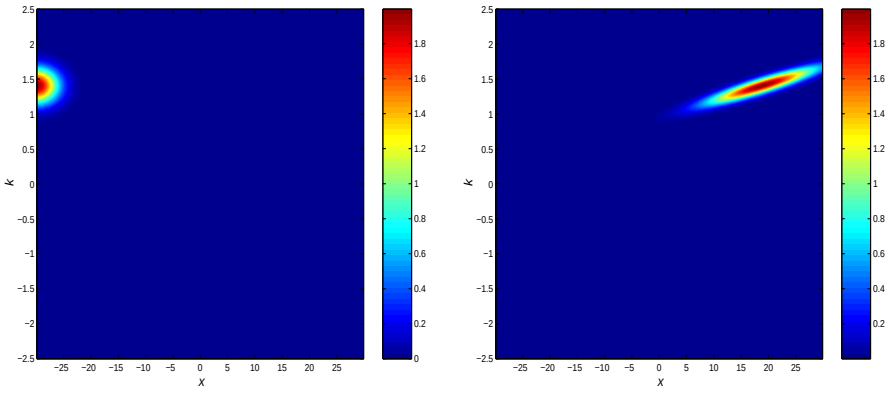

(a) $t=0$ (b) $t=20$

Figure 4: Example 4.1. The time evolution of a Gauss wave packet (GWP) in the free space.

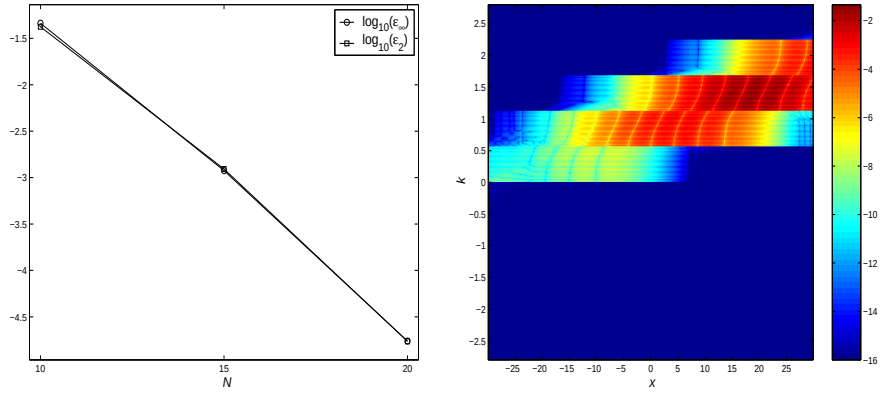

(a) (b)

Figure 5: Example 4.1. (a): the convergence history with respect to N; (b): $\Delta f(x,k)$ with $N=10$, $\log_{10}(\varepsilon_2)\simeq -1.37$ and $\log_{10}(\varepsilon_\infty)\simeq -1.34$.

and $k_0=1.4$ for Case III. By employing the mesh of the same size as here (i.e., $N=10$), it was found that the errors for the FDMs are (see Table 5.1 in [11]): 2.90%−10.7% for Case I; 15.6%−40.0% for Case II; and 19.3%−47.3% for Case III. For comparison, the proposed conservative cell average SEM produces errors under 1% for all three cases. Taking Case III as an example, we plot the GWP at $t=0$ and $t=20$ in Fig. 4. We observe there that, the GWP is broadened in the free space due to dispersion, i.e., the packet increases its spatial size. The absolute difference $\Delta f(x,k)$ at $t=20$ is presented in the right plot of Fig. 5, from which we can see that the biggest errors exist in the area where the peak of GWP is located. By refining the mesh, we obtain the spectral convergence of ε_2 and ε_∞ shown in the left plot of Fig. 5. For those three cases, our method has achieved an error under $10^{-4.5}$ at $t=20$ with the mesh $N=20$.

Therefore, we conclude that the accuracy of FDMs is far lower than that of the conser-

vative cell average SEM for the transient Wigner equation in the free space. In addition, the proposed SEMs deal with the inflow/outflow boundary conditions with high accuracy as usual for spectral collocation methods and the numerical solutions are free of pollution coming from the boundary treatments.

Example 4.2. In this example, we let a GWP with kinetic energy $E_0 \approx 1.12$ (corresponding to the GWP used in Case III of Example 4.1) to hit a Gaussian barrier with three different heights H. The Gaussian barrier with a width w is given in Fig. 6

$$V(x) = H\exp\left(-\frac{x^2}{2w^2}\right). \tag{4.3}$$

We investigate the capability of our algorithm in simulating the scattering of the GWPs by the barriers. Take $x_{\min} = -30$, $x_{\max} = 30$, $R = 20$ and $Q = 10$.

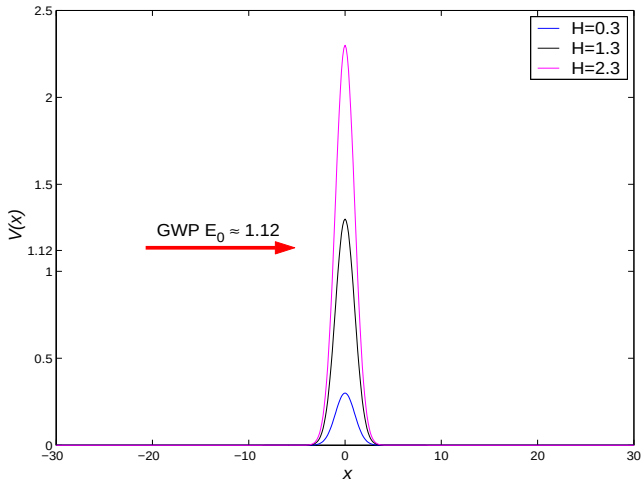

Figure 6: Example 4.2. The Gaussian barrier with the three kinds of height $H = 0.3, 1.3$ and 2.3. The energy of the incident GWP, saying E_0, is about 1.12 and $w = 1$.

First, we conduct a uniform mesh simulation with $N_{q,r} = M_{q,r} \equiv N$ for all r and q. As mentioned in Section 2, we should be very careful in evaluating (3.10), as we do not know before hand how large the truncation length Y should be used in (2.14). According to (2.17), we need to set the computational domain in the k-space as $k_{\min} = -\pi/(2\Delta y)$ and $k_{\max} = \pi/(2\Delta y)$, if $\Delta y = 0.3$. The question is how to find out a suitable value of N_y which defines the truncation length $Y = N_y \Delta y$. For the potential barrier considered here, there is a simple way to find this out. For a given mesh point $\{x_{i;q,r}, y_\mu\}, 1 \le i \le N, 1 \le \mu \le N_y$ defined in (2.15b) and (3.1a), we can consider the matrix $\chi(x_{i;q,r}, y_\mu)$ given in (3.11a). It is noted that for barrier potentials with a local support, the matrix

$$\left(\chi(x_{i;q,r}, y_\mu)\right)_{1\le i\le N, 1\le \mu\le N_y},$$

will be sparse and its entries become zero for compact potentials or extremely small for fast decaying potentials as μ goes to infinity. Therefore, we can relate the number of nonzero elements to the size of the support by observing how this number behaves if increasing μ. Once this number keeps unchanged, we will know we have a large enough N_y. Taking $H=0.3$ as an example, we show the curves of the number of nonzero elements of $\chi(x_{i;q,r},y_\mu)$,$1\le i\le N$,$1\le\mu\le N_y$ with respect to μ for different expansion orders in Fig. 7, where a matrix entry less than 10^{-16} is regarded as zero. We find there that the number of nonzero elements becomes unchanged if $\mu\ge 127$. Hence we set $N_y=127$ for the case $H=0.3$. However, for more general potentials with global support such as a fixed bias for electronic devices, we should make sure that the numerical solution converges as $N_y\to+\infty$, which means even larger N_y will be taken so that the resulting numerical solution is almost unchanged if increasing N_y.

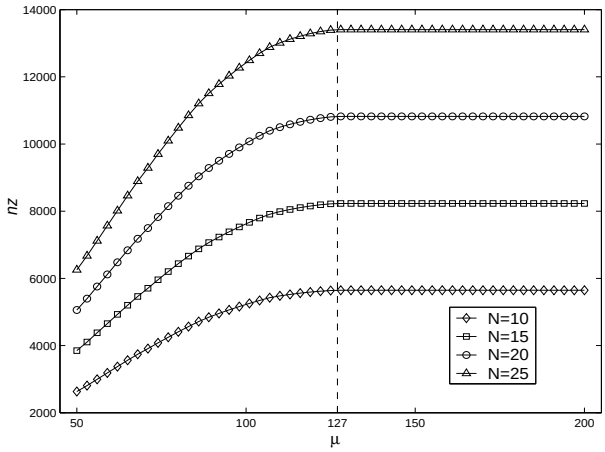

Figure 7: Number of nonzeros vs N_y.

Now, the numerical solution on the finest mesh is chosen to be the reference one. The mesh size of the reference solution for the case $H=0.3$ is $N=25$ and $N=30$ for both $H=1.3$ and 2.3. We observe during the interaction: (a) the GWP travels through the barrier easily in Fig. 8; (b) it is separated into two wave packets which move away from each other in Fig. 9; (c) it is almost completely reflected by the barrier in Fig. 10; and (d) in all three cases, many small oscillations appear around $k=0$ and the Wigner function takes negative values in some areas [14,19]. Three different scattering phenomena appear corresponding to three barrier heights.

We plot the convergence history with respect to N in Fig. 11. It is easily seen that the SEM converges rapidly for all three cases. Taking the case $H=2.3$ as an example, we plot $\Delta f(x,k)$ with the numerical solution calculated in a uniform mesh with an expansion order $N=25$, where we find that the biggest errors exist in the area around $k=0$, which corresponds to the small oscillations observed in Figs. 8, 9 and 10.

Next, we present the numerical results of the p-adaptive conservative SEMs. The initialization parameters are $\epsilon_T=10^{-4}$,$Z_0=1$,$T=20$; $\forall q,r,A^0_{q,r}=2,B^0_{q,r}=1,\check{M}^0_{q,r}=\check{N}^0_{q,r}\equiv N$,

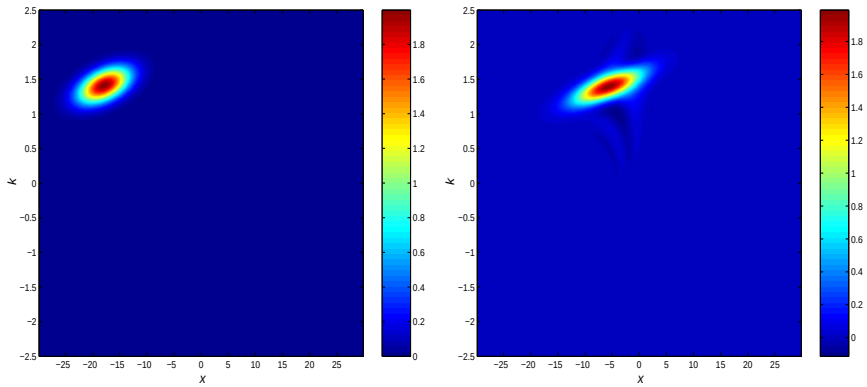

(a) $t=5$ (b) $t=10$

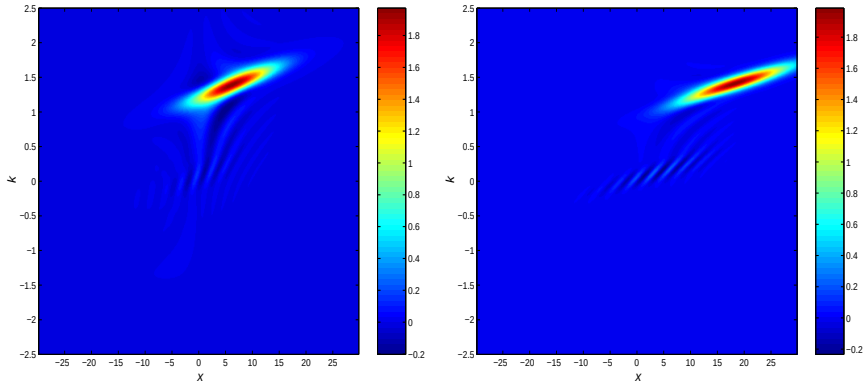

(c) $t=15$ (d) $t=20$

Figure 8: Example 4.2. The Wigner functions at different instants for the GWP interacting with the Gauss barrier. Since the barrier hight ($H=0.3$) is far less than the energy of GWP ($E_0\approx 1.12$), the GWP travels across the barrier easily.

where we set $N=25$ for the case $H=0.3$ and $N=30$ for both $H=1.3$ and 2.3. Conveniently, we use a fixed time step Δt. The results are listed in Table 2. We could observe the following: (a) the errors are under 10^{-2} as we expected while setting the tolerance $\epsilon_T=10^{-4}$; (b) the ratio $\check{\mathcal{N}}_{\max}/\mathcal{N}^{\text{ref}}$ is about 6.92%, 8.17% and 7.95% for $H=0.3,1.3,2.3$, respectively,

Table 2: Example 4.2. Numerical results for the p-adaptive conservative SEMs. Δt is the time step and $\check{\mathcal{T}}$ is the total steps needed in time with the final time $T=20$; $\check{\mathcal{N}}_{\max}=\max_n \check{\mathcal{N}}^n$ and $\check{\mathcal{N}}_T$ is the total cost at the final time step; $\check{M}_{\max}=\max_{q,r,n}\check{M}^n_{q,r}$ and $\check{N}_{\max}=\max_{q,r,n}\check{N}^n_{q,r}$; $A_{\max}=\max_{q,r,n}A^n_{q,r}$ and $B_{\max}=\max_{q,r,n}B^n_{q,r}$.

H	Δt	$\check{\mathcal{T}}$	$\check{\mathcal{N}}_{\max}$	$\check{\mathcal{N}}_T$	$\check{M}_{\max}$	$\check{N}_{\max}$	$A_{\max}$	$B_{\max}$	$\log_{10}(\varepsilon_2)$	$\log_{10}(\varepsilon_\infty)$
0.3	$\frac{1}{300}$	6137	8994	8990	20	24	6	4	−2.42	−2.31
1.3	$\frac{1}{500}$	10264	15193	15031	25	29	6	6	−2.25	−2.39
2.3	$\frac{1}{500}$	10305	14781	14588	25	30	8	7	−2.06	−2.16

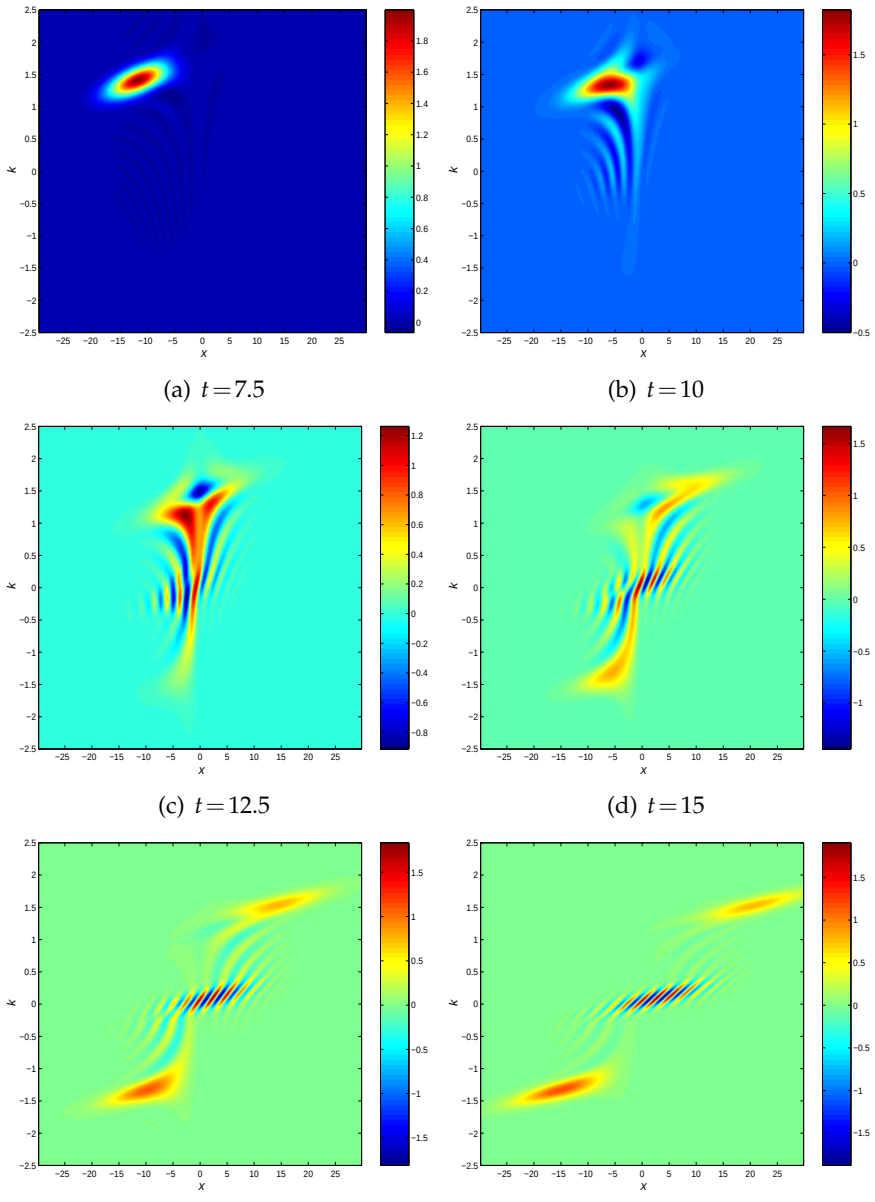

(a) $t=7.5$ (b) $t=10$

(c) $t=12.5$ (d) $t=15$

(e) $t=17.5$ (f) $t=20$

Figure 9: Example 4.2. The Wigner functions at different instants for the GWP interacting with the Gauss barrier. Since the barrier height ($H=1.3$) is comparable with the energy of GWP ($E_0\approx 1.12$), the GWP is separated into two wave packets: one traveling across the barrier while the other being reflected by the barrier.

which means that no more than 8.2% of collocation points from the uniform mesh for the reference solution are needed; (c) due to the restarting procedure for adjusting the buffer size $\{A^n_{q,r},B^n_{q,r}\}$, the price we pay for this adjustment method is the extra restarting steps

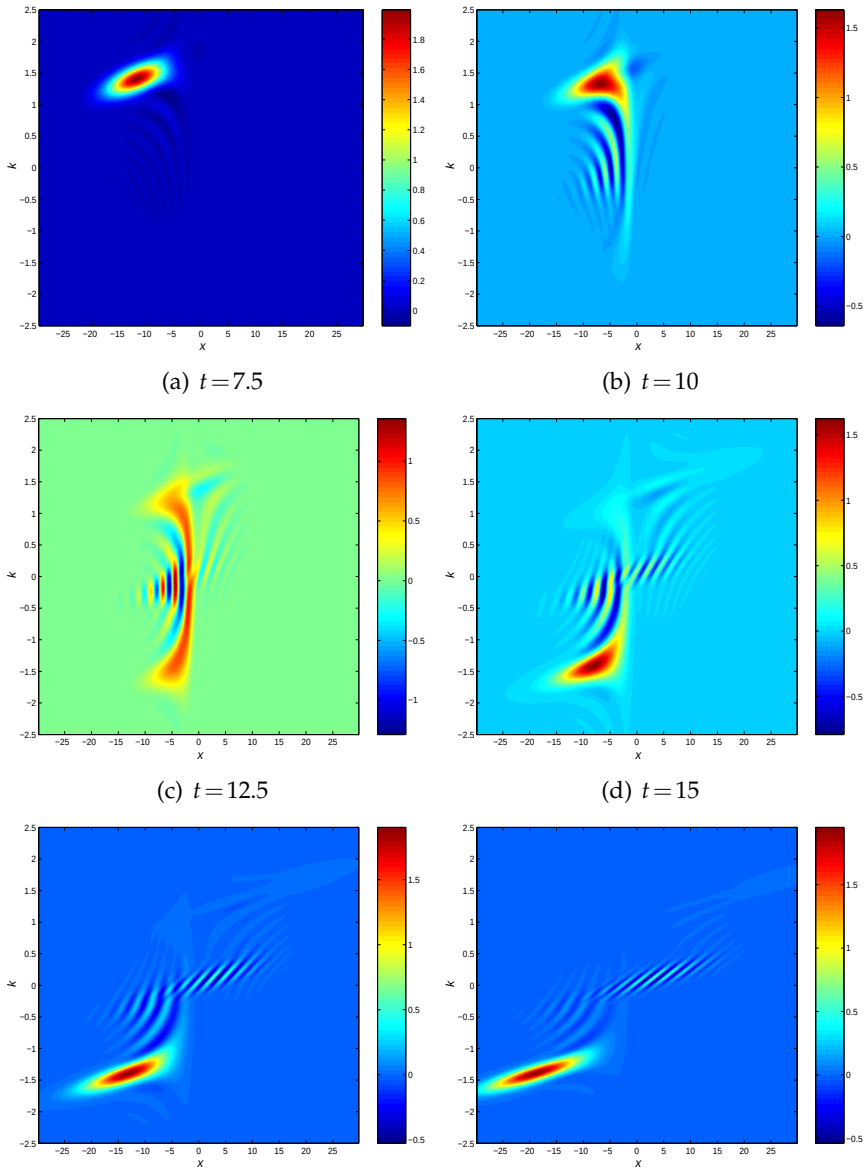

(a) $t=7.5$ (b) $t=10$

(c) $t=12.5$ (d) $t=15$

(e) $t=17.5$ (f) $t=20$

Figure 10: Example 4.2. The Wigner functions at different instants for the GWP interacting with the Gauss barrier. Since the barrier height ($H=2.3$) is far greater than the energy of GWP ($E_0\approx 1.12$), the GWP is almost completely reflected by the barrier.

needed in time, which are under 3.1% of the steps

$$\mathcal{T} := \frac{T}{\Delta t},$$

for those three cases, i.e., $\check{\mathcal{T}}/\mathcal{T} < 1.031$; and (d) the mesh size for the case $H=1.3$ is the

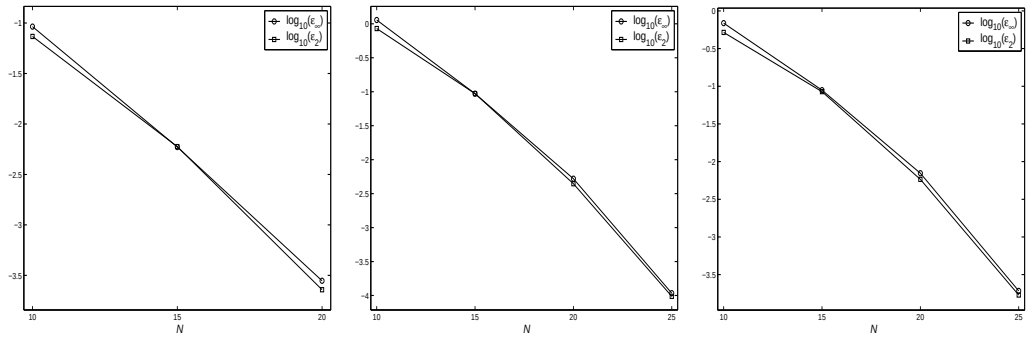

(a) $H=0.3$ (b) $H=1.3$ (c) $H=2.3$

Figure 11: Example 4.2. Convergence history with respect to N.

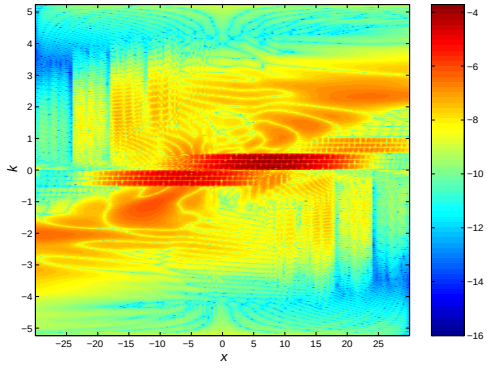

Figure 12: Example 4.2. $H=2.3$. $\Delta f(x,k)$ at $t=20$ with the numerical solution calculated with the truncation order $N=25$. $\log_{10}(\varepsilon_2)\approx -3.77$ and $\log_{10}(\varepsilon_\infty)\approx -3.72$. The biggest errors appear around $k=0$.

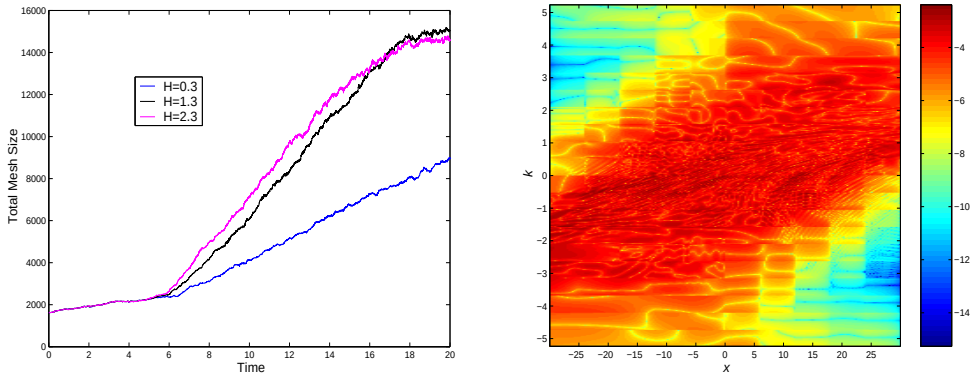

(a) (b)

Figure 13: Example 4.2. (a): the curves for the total mesh size $\check{\mathcal{N}}^n$ vs time t_n; (b): $\Delta f(x,k)$ at $T=20$ for the case $H=1.3$ with $\log_{10}(\varepsilon_2)\approx -2.25$ and $\log_{10}(\varepsilon_\infty)\approx -2.39$.

biggest among those three, which possibly reflects the separation of the GWP, i.e., more collocation points needed for two diverging wave packets. The increasing of the mesh size for the separation is confirmed in the left plot of Fig. 13 and this separation appears

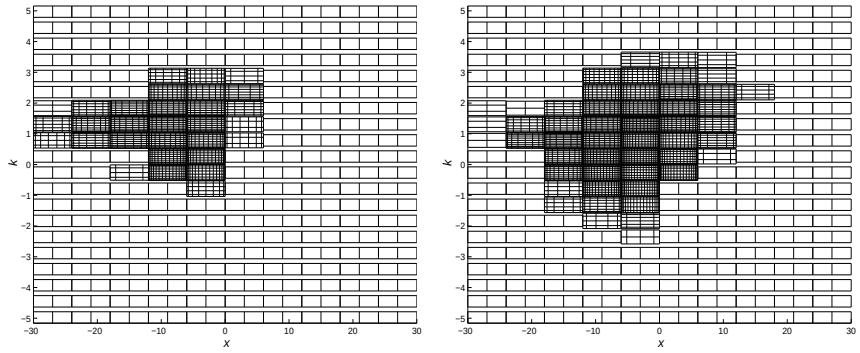

(a) $t=7.5, \check{\mathcal{N}}=3743, \check{M}_{\max}=17, \check{N}_{\max}=13$ (b) $t=10, \check{\mathcal{N}}=6079, \check{M}_{\max}=21, \check{N}_{\max}=14$

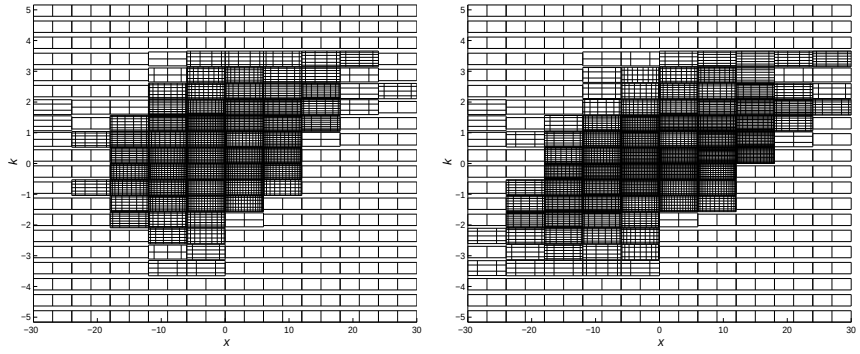

(c) $t=12.5, \check{\mathcal{N}}=8862, \check{M}_{\max}=21, \check{N}_{\max}=15$ (d) $t=15, \check{\mathcal{N}}=11753, \check{M}_{\max}=23, \check{N}_{\max}=19$

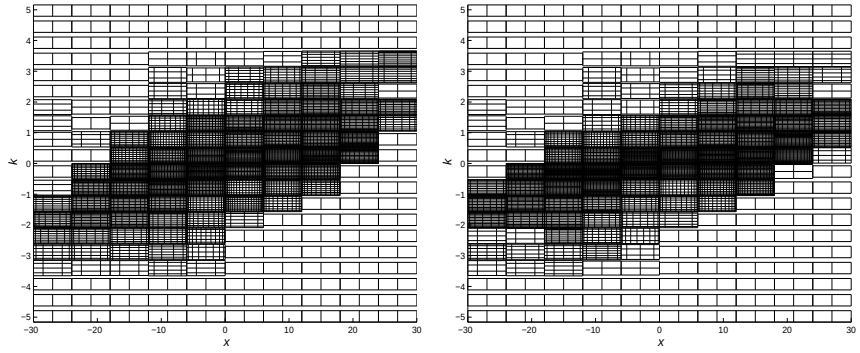

(e) $t=17.5, \check{\mathcal{N}}=14518, \check{M}_{\max}=21, \check{N}_{\max}=24$ (f) $t=20, \check{\mathcal{N}}=15031, \check{M}_{\max}=22, \check{N}_{\max}=29$

Figure 14: Example 4.2. The meshes used at different instants for the case $H=1.3$. The related Wigner functions are shown in Fig. 9.

at around $t=16$ (see (c–f) of Fig. 9). We also plot the error distribution $\Delta f(x,k)$ at $T=20$ for the case $H=1.3$ in Fig. 13, where we find that the biggest errors cluster in about three regions containing two wave packets and small oscillations around $k=0$ (refer to (f) of Fig. 9). The meshes at different instants for the case $H=1.3$ are shown in Fig. 14,

while the related Wigner functions are plotted in Fig. 9, from which we conclude that our p-adaptive methods capture the movement of GWP accurately and efficiently.

Remark 4.1. In all above numerical simulations, we find that the quantity $\Theta(x,t)$ in (3.13) is around the machine resolution, for example, 10^{-15} for double precision. This is expected from our conservative schemes, which maintains the mass conservation of the numerical solution exactly.

5 Discussions and conclusions

A strictly conservative adaptive spectral element method based on cell averages and point values of the Wigner distribution is proposed. Due to the analytical relation between the cell averages (local electron density) and point values, the proposed method ensures the exact mass conservation of electrons for the numerical solutions. With the help of fast sine and cosine transforms, efficient and highly accurate numerical results on adaptive meshes show potential of the proposed method in reducing the cost of computing the high-dimensional Wigner equations while maintaining electron conservation to high accuracy.

It should be noted that the overall accuracy of the proposed spectral method is limited by the smoothness of the Wigner distribution functions in the phase space and also the accuracy from the quadrature discretization of the Wigner potential in (2.15a). The strict electron conservation of the cell average spectral solution is obtained only for the discretized Wigner potential V_w^h in (2.15a).

By exploiting tensor product basis functions, the extension of the present adaptive conservative SEM into high-dimensional cases is straightforward and will be reported in a future work.

Acknowledgments

S. H. Shao is partially supported by China Scholarship Council (CSC) and he also thanks Dr. Biegel for providing the reference [12]. T. Lu is sponsored by SRF for ROCS, SEM and gratefully acknowledges the NSFC (Grant No. 10701005) and the support of NKBRP 2006 CB302705. W. Cai thanks the support of the United States Army Research Office (Grant No. W911NF-07-1-0492) and a NSFC support (No. 10828101). Additionally, the authors would like to thank the anonymous referees for their constructive comments and pointing out [25,26,31] to improve this work.

Appendix: Calculation of the oscillatory integrals $O_n(z)$

The oscillatory integrals are defined as

$$O_n(z) = \int_{-1}^{1} \mathrm{e}^{\mathrm{i}zx} T_n(x) \mathrm{d}x. \tag{A.1}$$

First, we exploit the expansion of e^{izx} in terms of the spherical Bessel functions of the first kind $j_k(z)$ and the Legendre polynomials $P_k(x)$ (see [36, Eq. (10.1.47)])

$$e^{izx}=\sum_{k=0}^{\infty}(2k+1)i^k j_k(z)P_k(x), \tag{A.2}$$

and then we have

$$\int_{-1}^{1}e^{izx}P_n(x)dx=2i^n j_n(z), \tag{A.3}$$

where we have used the orthogonality relation

$$\int_{-1}^{1}P_n(x)P_k(x)=\frac{2}{2n+1}\delta_{n,k}. \tag{A.4}$$

Second, we can express the Chebyshev polynomials $T_n(x)$ using the Legendre polynomials $P_k(x)$ as

$$T_n(x)=\sum_{k=0}^{n}c_{k,n}P_k(x), \tag{A.5}$$

where the coefficient $c_{k,n}$ is defined by

$$c_{k,n}=\frac{2k+1}{2}\int_{-1}^{1}T_n(x)P_k(x)dx, \tag{A.6}$$

and has a recurrence relation

$$c_{0,n}=\begin{cases}0, & n=1,\\ \dfrac{1}{2}\cdot\dfrac{1+(-1)^n}{1-n^2}, & n\neq 1,\end{cases}\qquad c_{1,n}=\begin{cases}0, & n=2,\\ \dfrac{3}{2}\cdot\dfrac{-1+(-1)^n}{n^2-4}, & n\neq 2,\end{cases} \tag{A.7a}$$

$$c_{k+2,n}=\begin{cases}0, & k=n-3,\\ \dfrac{2k+5}{2k+1}\cdot\dfrac{n^2-k^2}{n^2-(k+3)^2}\cdot c_{k,n}, & k=0,1,2,\cdots,n-4,n-2.\end{cases} \tag{A.7b}$$

Therefore, we get the final formula [37]

$$O_n(z)=\int_{-1}^{1}e^{izx}\Big[\sum_{k=0}^{n}c_{k,n}P_k(x)\Big]dx=\sum_{k=0}^{n}c_{k,n}\int_{-1}^{1}e^{izx}P_k(x)dx=2\sum_{k=0}^{n}i^k c_{k,n}j_k(z). \tag{A.8}$$

References

[1] E. Wigner, On the quantum corrections for thermodynamic equilibrium, Phys. Rev., 40 (1932), 749–759.
[2] C. Zachos, Deformation quantization: quantum mechanics lives and works in phase-space, Int. J. Mod. Phys. A., 17 (2002), 297–316.

[3] J. Hancock, M. A. Walton and B. Wynder, Quantum mechanics another way, Eur. J. Phys., 25 (2004), 525–534.
[4] C. Jacoboni, R. Brunetti, P. Bordone and A. Bertoni, Quantum transport and its simulation with the Wigner-function approach, Int. J. High. Speed. Electron. Syst., 11 (2001), 387–423.
[5] C. Jacoboni and P. Bordone, The Wigner-function approach to non-equilibrium electron transport, Rep. Prog. Phys., 67 (2004), 1033–1071.
[6] H. Kosina, Wigner function approach to nano device simulation, Int. J. Comput. Sci. Eng., 2 (2006), 100–118.
[7] V. Sverdlov, E. Ungersboeck, H. Kosina and S. Selberherr, Current transport models for nanoscale semiconductor devices, Mat. Sci. Eng. R., 58 (2008), 228–270.
[8] W. R. Frensley, Wigner-function model of a resonant-tunneling semiconductor device, Phys. Rev. B., 36 (1987), 1570–1580.
[9] W. R. Frensley, Boundary conditions for open quantum systems driven far from equilibrium, Rev. Mod. Phys., 62 (1990), 745–791.
[10] K. L. Jensen and F. A. Buot, The methodology of simulating particle trajectories through tunneling structures using a Wigner distribution approach, IEEE Trans. Electron. Devices., 38 (1991), 2337–2347.
[11] B. A. Biegel, Quantum Electronic Device Simulation, Ph.D. Thesis, Stanford University, 1997.
[12] B. A. Biegel, SQUADS Technical Reference, Unpublished, Stanford University, 1996.
[13] W. R. Frensley, Effect of inelastic processes on the self-consistent potential in the resonant-tunneling diode, Solid. State. Electron., 32 (1989), 1235–1239.
[14] N. C. Kluksdahl, A. M. Kriman, D. K. Ferry and C. Ringhofer, Self-consistent study of the resonant-tunneling diode, Phys. Rev. B., 39 (1989), 7720–7735.
[15] P. J. Zhao, Wigner-Poisson Simulation of Quantum Devices, Ph.D. Thesis, Stevens Institute of Technology, 2000.
[16] G. Ferrari, Effect of Contact Proximity on Quantum Transport in Mesoscopic Semiconductor Systems, Ph.D. Thesis, Università degli studi di Modena e Reggio Emilia, 2004.
[17] R. Kosik, Numerical Challenges on the Road to NanoTCAD, Ph.D. Thesis, Institute for Microelectronics, TU Vienna, 2004.
[18] M. Nedjalkov, H. Kosina, S. Selberherr, C. Ringhofer and D. K. Ferry, Unified particle approach to Wigner-Boltzmann transport in small semiconductor devices, Phys. Rev. B., 70 (2004), 115319.
[19] L. Shifren, C. Ringhofer and D. K. Ferry, A Wigner function-based quantum ensemble Monte Carlo study of a resonant tunneling diode, IEEE Trans. Electron. Devices., 50 (2003), 769–773.
[20] D. Querlioz, J. Saint-Martin, V. N. Do, A. Bournel and P. Dollfus, A study of quantum transport in end-of-roadmap DG-MOSFETs using a fully self-consistent Wigner Monte Carlo approach, IEEE Trans. Nanotechnol., 5 (2006), 737–744.
[21] C. Ringhofer, A spectral method for the numerical simulation of quantum tunneling phenomena, SIAM J. Numer. Anal., 27 (1990), 32–50.
[22] C. Ringhofer, A spectral collocation technique for the solution of the Wigner-Poisson problem, SIAM J. Numer. Anal., 29 (1992), 679–700.
[23] A. Arnold and C. Ringhofer, Operator splitting methods applied to spectral discretizations of quantum transport equations, SIAM J. Numer. Anal., 32 (1995), 1876–1894.
[24] A. Arnold and C. Ringhofer, A operator splitting method for the Wigner-Poisson problem, SIAM J. Numer. Anal., 33 (1996), 1622–1643.
[25] T. Goudon, Analysis of a semidiscrete version of the Wigner equation, SIAM J. Numer. Anal., 40 (2002), 2007–2025.

[26] T. Goudon and S. Lohrengel, On a discrete model for quantum transport in semi-conductor devices, Transport. Theor. Statist. Phys., 31 (2002), 471–490.
[27] W. Cai, D. Gottlieb and C. W. Shu, Essentially nonoscillatory spectral Fourier methods for shock wave calculations, Math. Comput., 52 (1989), 389–410.
[28] W. Cai, D. Gottlieb and A. Harten, Cell averaging Chebyshev methods for hyperbolic problems, Comput. Math. Applic., 24 (1992), 37–49.
[29] S. Gottlieb and C. W. Shu, Total variation diminishing Runge-Kutta schemes, Math. Comput. 67 (1998), 73–85.
[30] R. K. Pathria, Statistical Mechanics, 2nd Edition, Butterworth-Heinemann, Oxford, 1996.
[31] P. A. Markowich, C. A. Ringhofer and C. Schmeiser, Semiconductor Equations, Springer-Verlag, Wien-New York, 1990.
[32] J. P. Boyd, Chebyshev and Fourier Spectral Methods, 2nd Edition, Dover, New York, 2001.
[33] W. H. Press, S. A. Teukolsky, W. T. Vetterling and B. P. Flannery, Numerical Recipes in FORTRAN: The Art of Scientific Computing, 2nd Edition, Cambridge University Press, Cambridge, 1992.
[34] P. N. Swarztrauber, FFTPACK (version 4), 1985, `http://www.netlib.org/fftpack/`.
[35] L. Demeio, Splitting-scheme solution of the collisionless Wigner equation with non-parabolic band profile, J. Comput. Electron., 2 (2003), 313–316.
[36] M. Abramowitz and I. A. Stegun, Handbook of Mathematical Functions with Formulas, Graphs and Mathematical Tables, 9th Edition, Dover, New York, 1972.
[37] P. K. Kythe and M. R. Schäferkotter, Handbook of Computational Methods for Integration, Chapman & Hall/CRC, New York, 2005.